



Effects of multiwalled carbon nanotube morphology on the synthesis and electrocatalytic performance of Pt supported by multiwalled carbon nanotubes



Abdulrahman O. Al-Youbi^a, J.L. Gómez de la Fuente^{b,*}, F.J. Pérez-Alonso^b,
Abdullah Y. Obaid^a, J.L.G. Fierro^b, M.A. Peña^b, M. Abdel Salam^a, S. Rojas^{b,*}

^a Chemistry Department, Faculty of Science, King Abdulaziz University, P.O. Box 80200, Jeddah 21589, Saudi Arabia

^b Grupo de Energía y Química Sostenibles, Instituto de Catálisis y Petroleoquímica, CSIC, C/ Marie Curie 2 L10, 28049 Madrid, Spain

ARTICLE INFO

Article history:

Received 10 September 2013

Received in revised form

22 November 2013

Accepted 25 November 2013

Available online 2 December 2013

Keywords:

Electrocatalysts

ORR

CNT

Diameter

Durability

ABSTRACT

The effect of the diameter of multiwalled carbon nanotubes (CNTs) during the synthesis of CNT-supported Pt (Pt/CNT) has been studied. Three different CNTs with mean diameters of 10, 20 and 60 nm were chemically treated in acidic media and used as supports for Pt nanoparticles. Features such as specific surface area and the degree of surface modification during the chemical treatment are strongly influenced by the diameter of the CNT. Those features are key aspects that determine the size and loading of the Pt particles immobilized onto the nanotubes. Therefore, the catalysts prepared using nanotubes with smaller diameters exhibit both higher Pt loading and dispersion. Consequently, the performance of the catalysts during the electrooxidation of CO and oxygen reduction reaction in acidic media varies with the diameter of the CNTs. Remarkably, the catalyst prepared on 60-nm diameter CNTs is the most stable during long-term use. This higher stability arises from both the superior stability of the larger Pt particles and the stronger anchorage of the Pt onto the CNTs with higher amounts of surface oxygen groups. The groups increase in number with increased CNT diameters.

© 2013 Elsevier B.V. All rights reserved.

1. Introduction

Carbon-supported Pt-based materials are the most active catalysts used in proton exchange membrane fuel cells (PEMFCs); however, features such as durability and the amount of Pt in the state-of-the-art Pt/C must be optimized to reach commercial viability. One strategy used to decrease the Pt loading is to produce smaller Pt particles and therefore increase its mass activity. Currently, the low efficiency of proton exchange membrane fuel cells (PEMFCs) arises primarily from the slow kinetics of the oxygen reduction reaction (ORR) on the carbon-supported Pt nanoparticles [1–3]. The activity of the Pt particles toward the ORR increases when the particle size increases, and ca. 3-nm Pt particles supported on mesoporous carbon are the most active catalysts for the ORR in acid media relative to their mass [4,5]. However, the performance of these Pt-based catalysts remains insufficient to meet the requirements for commercial fuel cells, especially the prerequisites for Pt loading and durability [3,6].

The metal phase does not solely determine the catalytic behavior in the ORR. Generally, the support exerts more control over the design of heterogeneous catalysts, especially when the active phase consists of expensive metals. Supporting metal particles on an adequate carrier maximizes the mass fraction of exposed active sites by stabilizing nanosized metal particles. In electrocatalysis, the ideal support combines maximum dispersion of Pt nanoparticles with the accommodation of high metal loadings, high electron conductivity and corrosion resistance within the cathode electrode of fuel cells [7]. Together, these requirements make the materials based on carbon black, especially Vulcan XC72R, the most popular supports because they are relative graphitic and exhibit high electronic conductivity [8]. Recent studies have highlighted the support's ability to improve the performance of ORR electrocatalysts, especially for corrosion resistance in the harsh oxidizing environment required by ORR [9]. A plethora of carbon-based materials, including carbon nanotubes (CNTs), graphene, carbon nanofibers, carbon nanocoils, aerogels, carbon nanohorns, and carbon nanocages, are possible alternatives to the mesoporous carbon black materials as PEMFC electrocatalyst supports [10–17]. The cathodes within PEMFCs become degraded during fuel starvation, as well as the start-up/shut-down processes, due to a combination of effects, including Pt aggregation caused by the Ostwald ripening mechanism, Pt dissolution and/or particle detachment caused by

* Corresponding author. Tel.: +34 91 585 4632; fax: +34 585 4760.

** Corresponding author. Tel.: +34 91 585 4778.

E-mail addresses: gofuen@icp.csic.es (J.L. Gómez de la Fuente), srojas@icp.csic.es (S. Rojas).

corrosion of the support at high potentials in oxygen-rich environments [18–20].

Carbon nanotubes have been studied previously as supports for PEMFC-based electrocatalysts [21,22]. When using CNTs as a support, the deposition method generating the highly dispersed metal particles on the surface is a major concern. Anchoring Pt onto CNTs occurs via π -complexation between the Pt^{2+} precursors and the >C=C< fragments on the support's surface. Because the amount of these reactive >C=C< fragments available at the nanotube surface is limited, depositing large amounts of metal precursor per unit surface area is hindered, as was previously discussed [23]. The most advanced strategy to overcome this issue is the functionalization of the nanotube surface using chemical or/and physical treatments to increase the number of available anchoring sites [24]. The roles of oxygen-containing surface groups have been studied by many researchers. Oxygen-containing functional groups anchor nanoparticles, allowing larger amounts of metallic nanoparticles to be deposited on the carbon surface [25]. However, although the presence of oxygen-bearing groups may not lead to more Pt incorporation, it increases the strength of the interaction between Pt particles and the support, stabilizing the catalysts [21,22,26,27]. Additionally, the surface functional groups increase the hydrophilicity of the electrocatalysts, favoring the diffusion of the reactants toward the active sites [28].

In the present study, a series of Pt/CNT electrocatalysts were prepared using CNTs with different diameters. The effects of the CNT diameter on the creation of oxygen-bearing surface groups, the generation of defects, the incorporation of Pt, their catalytic performance during both CO oxidation and ORR and their resistance to degradation has been studied.

2. Experimental procedure

2.1. Functionalization of carbon nanotubes and synthesis of electrocatalysts

Three different batches of multiwall carbon nanotubes were obtained from Shenzhen Nanotech Port Co., Ltd. (China) with mean diameters of 10 nm (CNT10), 10–20 nm (CNT20) and 60–100 nm (CNT60). The CNTs were treated in acid to eliminate impurities and create surface oxygen groups. The functionalization protocol was described elsewhere [22,29]. Briefly, the CNTs were dispersed in 100 mL of a sulfonitric mixture (5.5 M H_2SO_4 :3.0 M HNO_3) per gram of CNT and refluxed at 65 °C under N_2 atmosphere for 2 h. Afterward, the reaction vessel was cooled down to room temperature, filled with distilled water (ca. 500 mL) and stirred overnight. The solid was recovered by filtration and washed thoroughly with distilled water until the pH of the filtered water was approximately 6.0; the filtered CNTs were dried overnight at 100 °C; the suffix -t identifies the treated CNTs. The functionalized CNTs were used as the support for 20 wt.% Pt/CNT-t using the polyol method [22,30]. The functionalized CNT-ts were dispersed in ethylene glycol (EG) and ultrasonicated for 1 h. A 1.25 mmol solution of H_2PtCl_6 in EG was added dropwise to a suspension containing the CNT-t with vigorous stirring at 60 °C. The mixture was stirred for 1 h. Subsequently, a solution containing 12.5 mmol NaBH_4 in EG was added to the mixture to reduce the Pt precursor. The mixture was refluxed at 130 °C for 3 h to ensure total reduction of the Pt. The process was carried out under a N_2 atmosphere and kept at 50 °C under flowing N_2 overnight. The solid was recovered by centrifugation, washed thoroughly with ethanol and dried at 70 °C for 8 h.

2.2. Physicochemical characterization

X-ray diffraction (XRD) analysis was performed with an X-ray diffractometer from X'Pert Pro PANalytical. Bragg's angles (2θ)

between 20° and 90° were recorded at a rate of 0.04° per step with 20 s per step. The assignment of the diffraction lines to the corresponding crystalline phases was carried out by comparison with Powder Diffraction Files (PDF) from the International Centre for Diffraction Data (ICDD), a.k.a. Joint Committee on Powder Diffraction Standards (JCPDS).

X-ray photoelectron spectroscopy (XPS) analysis of the samples was performed with a PHOIBOS 150 9MCD spectrometer with Multi-Channeltron detector (9 channels) using Mg K α radiation ($h\nu = 1253.6$ eV) and an XRC-1000 X-ray gun. The kinetic energies of the photoelectrons were measured with a hemispherical electron analyzer working in constant pass energy mode. The background pressure in the analysis chamber was maintained below 1×10^{-9} mbar during data acquisition. The powder samples were pelletized and mounted on a support rod in the pretreatment chamber. The energetic regions of interest were scanned until an adequate signal-to-noise ratio was attained. The intensities were estimated by calculating the integral of each peak, as determined by the subtraction of a Shirley type background and the experimental curve fit with a combination of Lorentzian and Gaussian lines with variable proportions. The binding energies were calibrated relative to the C 1s peak from graphitic carbon at 284.6 eV.

Thermogravimetric (TG) analysis of the CNT and CNT-t samples and of the Pt/CNT-t catalysts was performed on a Mettler Toledo TGA/SDTA 851 apparatus. Typically, 30–40 mg of the sample was heated from 298 to 1373 K at 10 K min^{-1} under an atmosphere of air.

Surface specific area values were determined using the N_2 adsorption–desorption isotherms of samples at liquid N_2 temperatures with a Micromeritics ASAP 2000 apparatus. Samples were previously degassed at 423 K for 24 h. The specific areas were calculated by applying the BET method to portions of the isotherms within the $0.05 < P/P_0 < 0.30$ relative pressure range.

Raman spectra of the CNT and CNT-t were recorded using a single monochromator Renishaw in Via Raman Microscope System 1000 spectrometer equipped with a 100 mW laser with emission at 532 nm equipped with a thermoelectrically cooled CCD detector and a holographic super-Notch filter. The instrument was internally calibrated with a silicon reference at 520 cm^{-1} and had a peak position resolution of 1 cm^{-1} ; the spectrum acquisition time was 10 s, and 10 spectra were acquired to ensure an optimal signal to noise ratio.

The X-ray fluorescence analysis (TXRF) was performed with a Seifert EXTRA-II spectrometer, equipped with 2 X-ray fine focus lines, Mo and W anodes, and an Si(Li) detector with an 80 mm^2 active area and a 157 eV resolution at 5.9 keV (MnK α). Direct solid analysis was used to quantify the metal content in all electrocatalysts.

2.3. Electrochemical characterization

Electrochemical tests were conducted at room temperature using a three-electrode cell connected to a computer-controlled potentiostat/galvanostat (Autolab PGstat 302N). A graphite rod was used as the counter electrode. The potentials were measured and reported against a reversible hydrogen electrode (RHE) in the supporting electrolyte. The electrocatalysts were deposited on a glassy carbon (GC) electrode (5 mm diameter) with an ink. Previously, the glassy carbon electrode was polished (0.05 μm alumina) to a mirror finish and rinsed with triply distilled water in an ultrasonic bath. The actual Pt loading deposited onto the working electrode was of $20 \mu\text{g}_{\text{Pt}} \text{ cm}^{-2}$. The appropriate amount of each catalyst (considering the actual Pt loading as determined from TXRF analysis) was dispersed in 3 mL of milliQ H_2O and 60 μL Nafion using sonication. Subsequently, 20 μL of the ink was dropped onto the electrode and dried under Ar.

Before the electrochemical tests, the electrolyte was sparged with bubbling Ar for at least 30 min. The electrocatalyst was conditioned via the following protocol: 40 cyclic scans from 0.05 to 1.2 V at 100 mV s⁻¹ and 10 further cyclic scans at 10 mV s⁻¹. For the CO_{ad} stripping analysis, carbon monoxide was adsorbed over 5 min at 50 mV from a CO-saturated 0.1 M HClO₄ electrolyte. After CO removal (30 min Ar purge), three consecutive cyclic voltammograms (0.05–1.2 V) were recorded at 10 mV s⁻¹.

To assess the stability of the catalysts, 3000 consecutive cyclic voltammograms between 0.6 V and 1.2 V at 100 mV s⁻¹ under Ar atmosphere were recorded. Subsequently, a further CO_{ad} stripping analysis was recorded as described above.

The performance of the catalysts during ORR was studied with conventional rotating disk electrode (RDE) techniques. The studied catalysts (deposited onto the GC electrode as described above) were immersed in an O₂-saturated 0.1 M HClO₄ electrolyte, and the potential was cycled between 1.1 V and 0.05 V at 20 mV s⁻¹ and 1600 rpm until the obtained current was stable. The kinetic parameters of the electrocatalysts were determined using the mass transport correction equation (Eq. (1)) generally employed for thin-film RDE experiments:

$$\frac{1}{j} = \frac{1}{j_k} + \frac{1}{j_d} \quad (1)$$

where j is the measured current density, while j_k and j_d are the kinetic and diffusion-limited current densities, respectively. To accurately compare the kinetic data, the current values were referenced to the real Pt surface area of the electrodes [31,32]. The real Pt surface area or electrocatalytic surface area (ECSA) of the electrodes was determined from CO_{ad} stripping experiments recorded immediately after the ORR experiments.

3. Results and discussion

3.1. Precursors and catalysts characterization

Fig. 1 presents the nitrogen adsorption–desorption isotherms of the functionalized nanotubes. All isotherms were Type IIb [33,34], exhibiting almost no hysteresis loop typical of non-porous (macro/mesoporous) solids [35]. In line with previous reports, a relationship between the specific area and nanotube diameters was observed, and the specific areas decreased in the following order: CNT10 > CNT20 > CNT60 [33,34]. Table 1 demonstrates that this trend also applies to the functionalized CNT-t.

Fig. 2 displays the thermogravimetric analysis profiles recorded in air for both fresh and functionalized carbon nanotubes, as well as the Pt/CNT electrocatalysts. The thermogravimetric profiles of the CNTs reveal a single weight loss at 450 °C for CNT10 and at 520 °C for CNT20 and CNT60. This severe weight loss accounts for the combustion of the carbon nanotubes [36]. The residual mass remaining after the combustion of the CNTs corresponds to the oxidized phase of the catalysts used during their preparation. The EDS

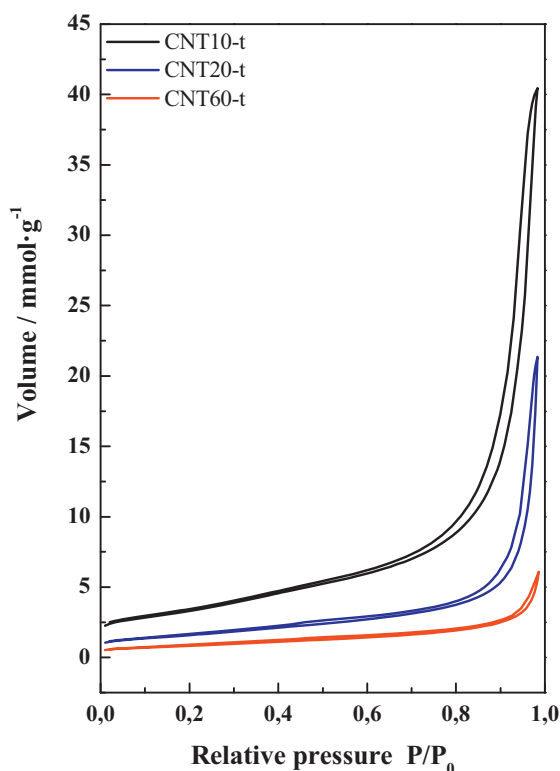


Fig. 1. N₂ adsorption–desorption isotherms of the functionalized CNT-t.

analysis of the fresh CNTs revealed the presence of cobalt in CNT10 and nickel in CNT20 and CNT60. The residual mass remaining after thermal treatment in air for CNT10 was of ca. 12 wt.%, while 2.1 and 4.3 were measured for CNT20 and CNT60, respectively. In line with previous reports, the larger amount of catalyst in CNT10 might explain its lower onset combustion temperature [36]. The thermogravimetric profiles of CNTs also display steep weight losses similar to the profiles recorded for the as-received carbon nanotubes. The treated nanoparticles undergo combustion beginning at higher temperatures, especially for CNT10-t. Additionally, the weight of the residual material from the functionalized samples (CNT-t) was lower than the residue from the fresh samples, indicating that the chemical treatment in acid medium removes some of the impurities from the CNTs.

The thermogravimetric (TG) profiles of the Pt/CNT-t are displayed in Fig. 2c. All samples record similar weight loss profiles: a single weight loss process with total weight losses ranging between 74 wt.% and 78 wt.%. The smaller weight losses are recorded for the Pt/CNT relative to the CNT-t because Pt was incorporated on the CNT-t. Additionally, taking into account the weight losses recorded for both the CNT-t and Pt/CNT-t, the TG analyses indicated that the

Table 1
Physicochemical data of the samples.

Catalyst	BET (m ² g ⁻¹)	Atomic ratios from XPS		Pt size (nm)		Pt loading (wt.%)
		O/C	Pt/C	XRD	TEM	
CNT10	213	0.003				
CNT20	131	0.018				
CNT60	51	0.022				
CNT10-t	269	0.016				
CNT20-t	128	0.021				
CNT60-t	67	0.025				
Pt/CNT10-t		0.024	0.012	5.7	3.5 ± 2.0	20.3
Pt/CNT20-t		0.033	0.016	7.0	3.8 ± 2.4	17.8
Pt/CNT60-t		0.042	0.007	8.3	6.8 ± 2.8	15.7

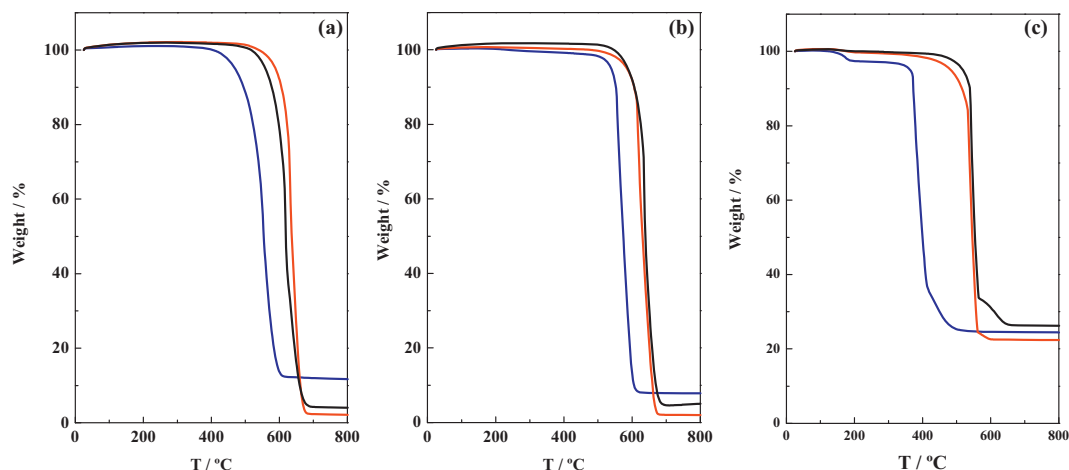


Fig. 2. Thermogravimetric profiles recorded in air of: (a) fresh nanotubes (b) chemically treated nanotubes (c) Pt/CNT-t. CNT10 series (blue line), CNT20 series (red line) and CNT60 series (black line). (For interpretation of the references to color in figure legend, the reader is referred to the web version of the article.)

amount of Pt incorporated onto the CNTs is as follows: Pt/CNT10-t > Pt/CNT20-t > Pt/CNT60-t. The most relevant difference between the thermogravimetric profiles of the Pt/CNT-t is the temperature where weight loss begins; this value shifts from ca. 500 °C for Pt/CNT20-t and Pt/CNT60-t to ca. 370 °C for Pt/CNT10-t. The lower onset temperature for the CNT10 is also observed in the TG profiles of CNT10 and CNT10-t but the incorporation of Pt seems to enhance the differences.

The actual Pt loadings of the Pt/CNTs were determined with TXRF and follow a decreasing trend: 20.3 wt.% on Pt-CNT10-t, 17.8 wt.% on Pt-CNT20-t and 15.7 wt.% on Pt-CNT60-t. The amount of Pt incorporated onto the CNT-t increases when the diameter of the CNTs decreases.

The surface composition and relative abundance of C, O and Pt in each samples was studied by XPS. The C 1s core-level region of the CNTs exhibits a broad peak comprising contributions from different C-species. The component at the lowest binding energy (284.6 eV)

is assigned to graphitic carbon and accounts for 70–78 at.% of the total carbon species. Two additional peaks at 286.5 and 287.5 eV are ascribed to C–OH and C–OOH species, respectively. When combined, these oxygenated species account for ca. 12–15 at.% of the total C. Finally, at higher binding energies (290.4 eV), a broad peak caused by $\pi \rightarrow \pi^*$ transitions characteristic of pure graphitic species and correlating with the amount of unsaturated C=C bonds (C_{π} sites) appears in the spectrum of each sample. This peak accounts for ca. 7–9% of the carbon in each studied sample.

The O/C surface atomic ratios (see Table 1) increase with the increasing diameters of the CNTs. The actual values are as follows: 0.003 for CNT10, 0.018 for CNT20 and 0.022 for CNT60. After functionalization, the O/C ratio increases for every sample, especially for the CNTs with the smallest diameters: 0.016 for CNT10-t, 0.021 for CNT20-t and 0.025 for CNT60-t. These results indicate that the diameter of the nanotubes critically affects their chemical functionalization.

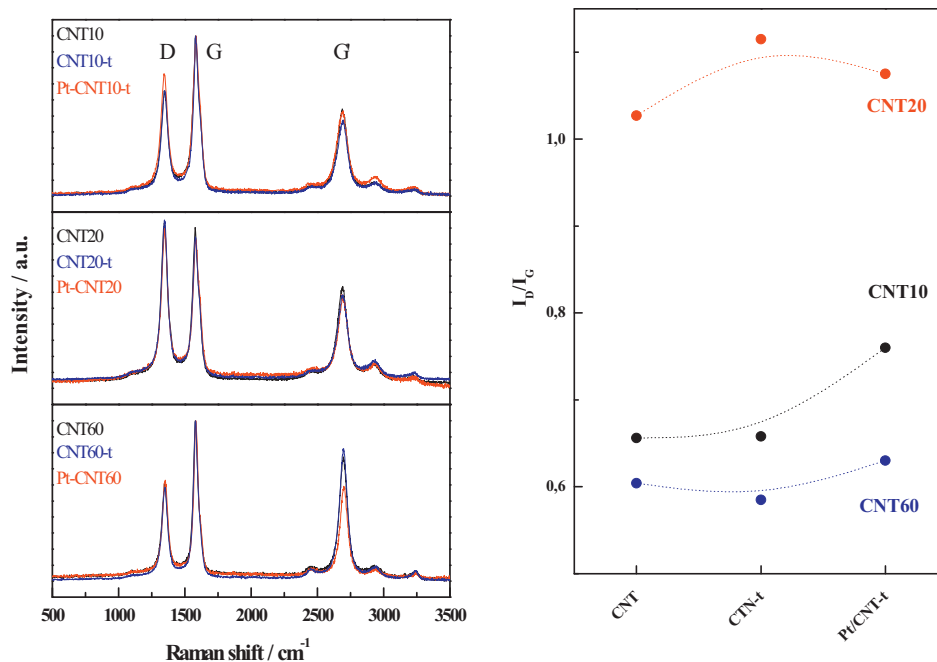


Fig. 3. Raman spectra of the fresh (black line), functionalized (blue line) and Pt-CNTs (red line). The left panel represents the variation of the I_D/I_G for all samples. (For interpretation of the references to color in figure legend, the reader is referred to the web version of the article.)

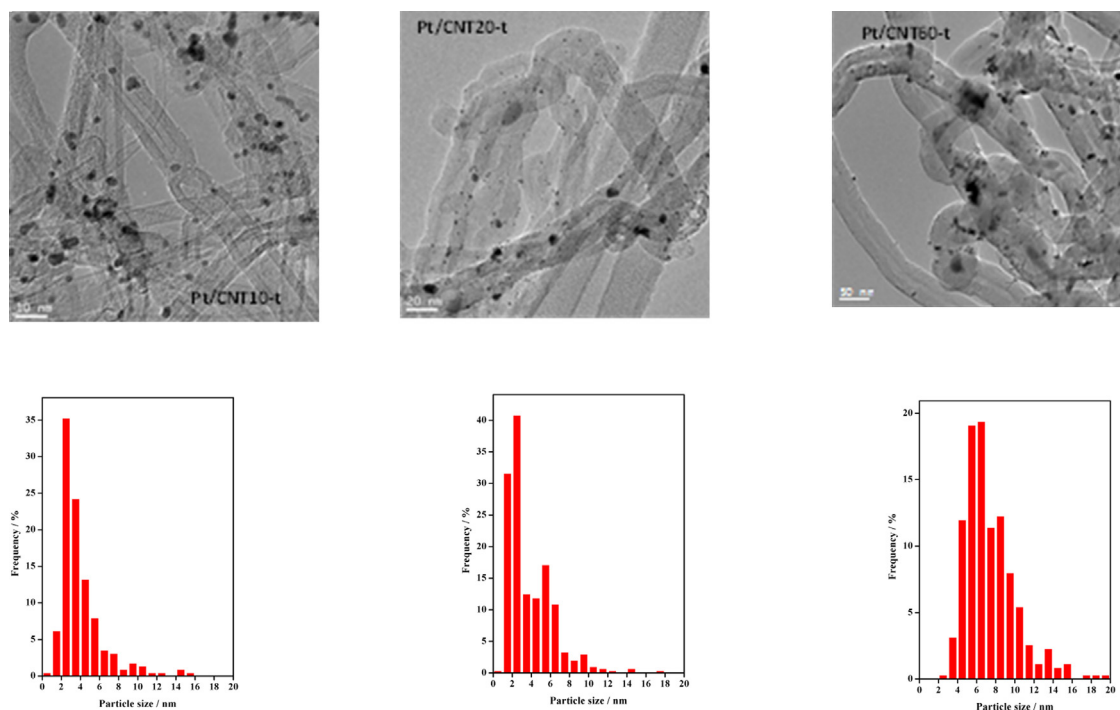


Fig. 4. Representative TEM images of Pt/CNT10-t, Pt/CNT20-t and Pt/CNT60-t and the corresponding histograms of particle sizes distribution.

The Pt 4f core-level region of each sample comprises 3 doublets with Pt 4f_{7/2} peak maxima at 71.1, 72.5 and 74.2 eV, indicating the presence of Pt⁰, Pt²⁺ and Pt⁴⁺ species, respectively. Pt/CNT10-t and Pt/CNT20-t exhibit similar Pt surface atomic ratios (Pt_{at}/C_{at}) of 0.012 and 0.015, respectively; this value drops to 0.007 for Pt/CNT60-t. Additionally, latter sample displays a ca. 80% ratio of Pt⁰ vs total Pt, dropping to ca. 70% for Pt/CNT10-t and Pt/CNT20-t. The XPS results indicate that Pt particles disperse better on the nanotubes with the smaller diameters and tend to form larger aggregates on Pt/CNT60-t.

Raman spectra of the fresh and functionalized carbon nanotubes are presented in Fig. 3a. The most prominent features in the every Raman spectrum are a set of bands at approximately 1348, 1580 and 2698 cm⁻¹ that are usually referred to as the D, G and G' (or 2D) bands [33,37]. The G band accounts for the presence of sp² hybridized carbon networks, i.e., graphitic structure. However, the D and the G' bands account for the presence of defects, including the edges of the nanotubes [38]. A weak band at ca. 1620 cm⁻¹ (D' band) accounting for disorder-induced features is observed in every Raman spectrum as a shoulder on the G peak. The quality of the nanotubes, i.e., their degree of disorder, as well as their evolution after chemical treatment and Pt incorporation, can be identified by following the changing intensities of the D, 2D and G bands [36]. In principle, the generation of defects increases the I_D/I_G ratio but decreases the I_{2D}/I_G ratio [33]. Fig. 3b presents the variation in the I_D/I_G ratios between all studied samples.

The I_D/I_G ratios and the large full width at the half maximum of the D peaks (approximately 68 cm⁻¹) have been previously reported for graphitized materials. The higher I_D/I_G ratio of CNT20 relative to the ratios for CNT10 and CNT60 suggest the presence of more defects in this sample. This trend also applies to CNT20-t and Pt/CNT20-t. The evolution of the I_D/I_G ratios presented in Fig. 3b indicates that the chemical treatment moderately increases the amount of defects in the nanotubes. The intensity of the D band was not expected to be affected by the amount of oxygen-bearing groups generated during the functionalization of the CNTs because this band correlates with the number of defects rather than the chemical state of the edge [33].

Fig. 4 depicts the X-ray diffractograms of all Pt/CNT-t catalysts. The characteristic reflections for the Pt fcc structure and a diffraction peak at ca. 25° ascribed to the (002) planes of graphite are the only ones observed in every Pt/CNT-t. Noticeably, the diffraction peak for graphite shifts to higher 2θ values as the diameter of the nanotubes increases, indicating the presence of lattice strain caused by the curvature of the nanotubes.

The average Pt grain size was determined by applying the Scherrer equation to the 200 reflection at ca. 67.7°. Although this reflection was not the most intense signal from the Pt fcc structure, it was chosen because it is not affected by the graphitic carbon 002, 100 and 110 reflections at 24.9°, 43.3° and 79.6°, respectively. Pt crystallite sizes of 8.3, 7.0 and 5.7 nm were calculated for Pt/CNT60-t, Pt/CNT20-t and Pt/CNT10-t, respectively, demonstrating a clear trend for increasing size with increasing CNT diameters.

Fig. 5 displays selected TEM micrographs of each Pt/CNT-t alongside the corresponding histograms of the particle size distributions constructed by counting at least 250 particles on each catalyst. The TEM images confirm that the diameter of the nanotubes increases: CNT60-t > CNT20-t > CNT10-t. Moreover, the mean size of the Pt particles in Pt/CNT10-t was ca. 3.5 nm, exhibiting a narrow size distribution of particle sizes. The mean Pt particle size in Pt/CNT20-t was 3.8 nm; however, the particle size distribution was broader than the distribution observed in Pt/CNT10-t, demonstrating a bimodal particle size distribution with maxima at ca. 3 and 6 nm. Pt/CNT60-t also displays a broad particle size distribution and a 6.8-nm mean particle size. These values agree with the crystallite sizes observed by XRD and confirm that the size of the Pt particles increases with the CNT diameter.

The characterization results clearly illustrate how features such as the specific surface area, the amount of surface oxygen-groups and the amount of defects are influenced by carbon nanotube diameter. Therefore, the specific surface area of the carbon nanotubes increases with their decreasing diameter. The opposite trend was observed, however, relative to the amount of surface oxygen groups (expressed as the O/C surface atomic ratio, see Table 1); this parameter increases with larger CNT diameters. The amount of Pt immobilized onto the treated nanotubes (CNT-t) follows a

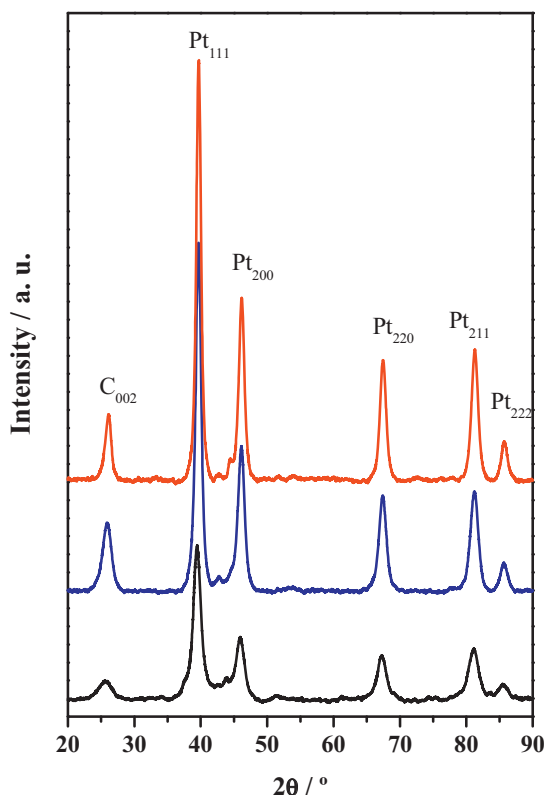


Fig. 5. X-ray diffractograms of Pt/CNT10-t (black line), Pt/CNT20-t (blue line) and Pt/CNT60-t (red line). The characteristic diffraction lines of the fcc structure of Pt and of the hexagonal structure of graphite are shown.

decreasing order: Pt/CNT-10 > Pt/CNT-20 > Pt/CNT60. The amount decreases with increasing nanotube diameters. Remarkably, the Pt crystallite size follows the opposite trend. Pt size increases with increasing carbon nanotube diameters; therefore, Pt loading and Pt size follow opposite trends. This observation seems counterintuitive because usually lower metallic loadings facilitate the formation of smaller particles. This effect may be rationalized by considering that the specific surface area of the carbon nanotubes increases when the nanotube diameter decreases, as illustrated in Table 1. Consequently, higher Pt loadings may be accommodated on the CNT-t with the smaller diameters, exposing a higher fraction of anchoring sites and therefore facilitating Pt dispersion. Additionally, Table 1 also illustrates that the degree of CNT-t functionalization, which is measured as the O_{at}/C_{at} , follows an increasing order: CNT10-t < CNT20-t < CNT60-t. Because both Pt loading and dispersion are improved in the CNTs with less surface oxygen groups, the oxygen-bearing groups are not the only sites capable of anchoring Pt particles. The XPS results also suggest that the amount of sp^2 carbon increases with decreasing CNT diameters. Previous proposals have also suggested that sp^2 sites, rather than O-bearing groups, are the preferential anchoring sites for well dispersed Pt particles on carbon support [22]. The incorporation of well dispersed Pd particles onto carbon supports has been discussed in similar lines concluding that the surface oxygen-containing groups are not capable to stabilize highly dispersed Pd particles [39]. Creating oxygen-bearing groups on the surface of mesoporous carbon or CNTs seems to facilitate the incorporation of higher amounts of metal, especially on CNTs. In fact, it is well documented that it is not possible to achieve Pt loadings above 20 wt.% with non-functionalized CNTs [21,22], and references therein. It has been proposed recently that the presence of oxygen-containing groups might reduce the electrostatic interaction between the Pt

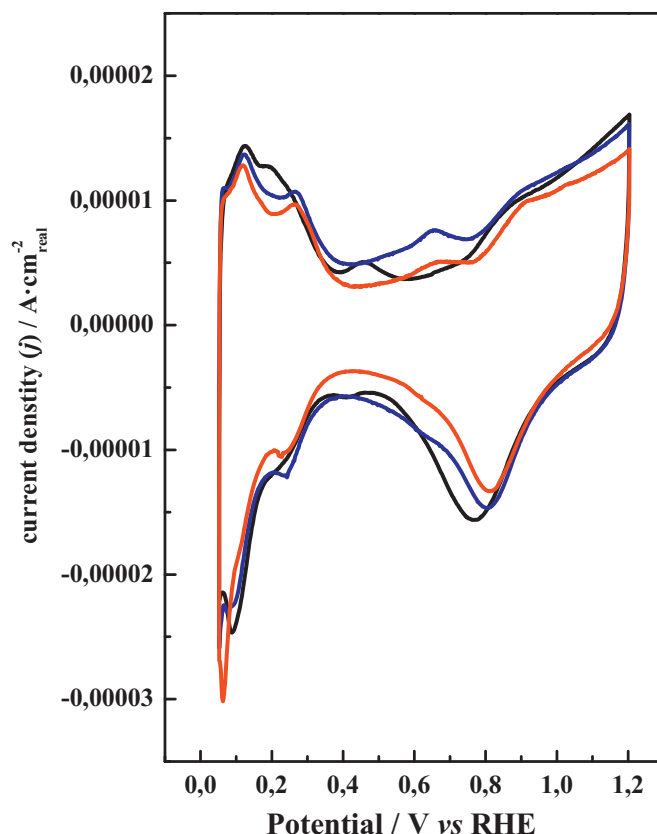


Fig. 6. Voltammograms of Pt/CNT10-t (black line), Pt/CNT20-t (blue line), and Pt/CNT60-t (red line) recorded in 0.1 M $HClO_4$ at 10 mV s^{-1} . (For interpretation of the references to color in figure legend, the reader is referred to the web version of the article.)

precursor and the modified support, leading to lower metallic dispersions [40]. However, it should be noted that the final strength of the Pt-support interaction is not necessarily defined by the strength of the interaction between the support and the metal precursor alone, but more importantly by features such as thermal treatments which lead to the final metal-support interaction. Besides, the actual nature of the metal precursor under the environment for the synthesis of the catalysts remains elusive making it difficult to determine accurately the observed trends in Pt dispersion with the support; i.e., the preferential observation of well dispersed Pt particles on non-functionalized support along with the formation of larger Pt aggregates and the broadened Pt size distributions on the CNTs with larger diameters, such as CNT20-t and CNT60-t.

3.2. Electrocatalytic performance for the CO_{ad} oxidation and ORR

Fig. 6 displays the cyclic voltammograms of the Pt/CNT recorded in 0.1 M $HClO_4$. To obtain accurate trends reflecting the hydrogen and OH adsorption/desorption processes affected by the variable Pt loadings, specific surface areas, and support capacitances, the voltammograms were normalized to the surface area of Pt determined from the CO_{ad} stripping analysis [41]. The typical features of Pt in $HClO_4$, i.e., the hydrogen adsorption–desorption region between 0.0 V and ca. 0.35 V, the double-layer region and, at potentials higher than 0.7 V, the region corresponding to the formation of adsorbed oxygen and the reduction of the oxide layer on Pt, are clearly observed for all catalysts. However, certain differences may be observed. First, the charge of the H_{upd} region appears to increase

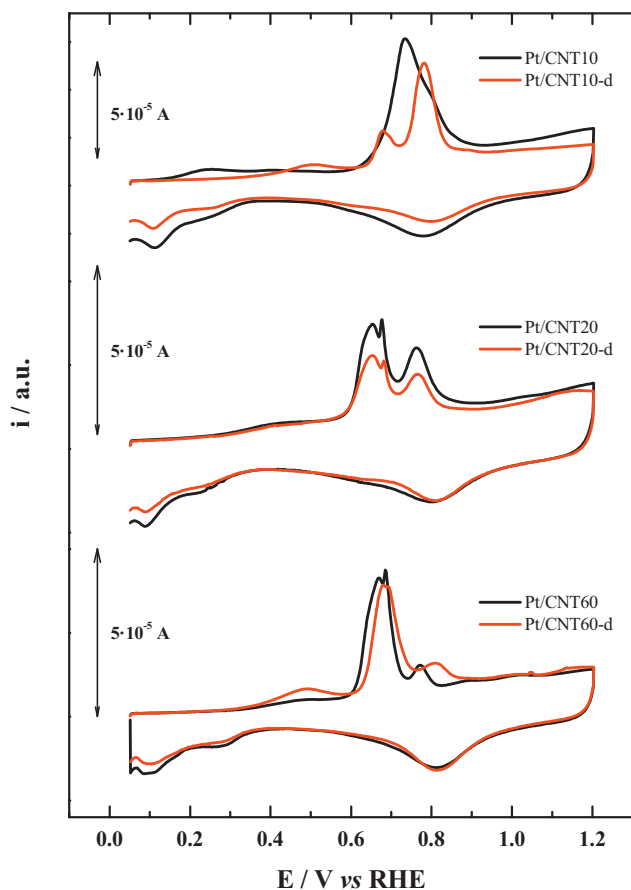


Fig. 7. Voltammograms for the electrooxidation of CO_{ad} for Pt/CNT-10 (upper panel), Pt/CNT-20 (middle panel) and Pt/CNT-60 (lower panel) recorded in 0.1 M HClO_4 at 10 mV s^{-1} before (black line) and after (red line) the stability tests. (For interpretation of the references to color in figure legend, the reader is referred to the web version of the article.)

with the decreasing Pt size. Additionally, increased currents in the double-layer region when the diameter of the CNTs decreased were observed.

Interestingly, the onset potential of the oxide formation region shifts toward less positive potentials as the Pt particle size decreases. This observation is more obvious when following the changing potential of the oxide reduction peaks: $\text{Pt/CNT60-t} > \text{Pt/CNT20-t} > \text{Pt/CNT10-t}$. This trend indicates that the oxophilicity of the samples increases with decreasing particle sizes [41].

Fig. 7 presents the voltammograms recorded during the CO_{ad} electrooxidation over the Pt/CNT-t catalysts. As expected, the voltammograms of the CO_{ad} stripping record no hydrogen features in the positive sweep; however, the hydrogen features appear in the reverse sweep, confirming the complete oxidation of CO_{ad} during the positive sweep. The CO_{ad} electrooxidation profile is unique for each catalyst; therefore, the electrooxidation of CO_{ad} over Pt/CNT10-t manifests a broad band with a maximum (E_{PCO}) at 730 mV. CO_{ad} oxidation over Pt/CNT20-t displays two well-defined peaks with E_{PCO} at 650 and 760 mV. The CO_{ad} stripping voltammogram of Pt/CNT60-t presents a main peak with E_{PCO} at 670 mV and a less intense peak at 770 mV. In addition, a distinct, though small, CO_{ad} oxidation prewave is observed at $E > 400 \text{ mV}$.

There is a strong consensus in that the profile, the onset potential and peak maxima of the CO_{ad} stripping peak may be used to indicate the crystallite and agglomeration sizes [23,26,41–43]. The electrooxidation of CO proceeds through a Langmuir–Hinshelwood

mechanism [23,43], where the OH_{ad} species form at Pt sites close to the Pt-CO_{ad} (Eq. (2)).



The formation of OH_{ad} species on Pt was favorable on the catalysts with smaller Pt crystallites, following an increasing potential order: $\text{Pt/CNT60-t} > \text{Pt/CNT20-t} > \text{Pt/CNT10-t}$. However, the onset potential for the CO_{ad} electrooxidation shifts toward more positive values as the Pt particle size decreases: $\text{Pt/CNT60-t} \sim \text{Pt/CNT20-t} < \text{Pt/CNT10-t}$. This observation may be rationalized by considering that the strength of the Pt–CO bond strongly influences the potential for the CO_{ad} stripping and increases with the decreasing crystallite size. The observation of two CO_{ad} electrooxidation peaks on Pt/CNT20-t and Pt/CNT60-t suggests a bimodal particle size distribution, validating the TEM data (see above). Therefore, the peak at less positive values accounts for the CO_{ad} oxidation on the larger Pt particles or on Pt agglomerates, while the smaller particles are responsible for the CO_{ad} oxidation at higher potentials [43]. However, the CO_{ad} electrooxidation over Pt/CNT10-t displays a single band with both onset and peak potentials located at more positive values, similar to the smaller Pt crystallites on Pt/CNT10-t.

The stability of the Pt/CNT-t was evaluated by subjecting the catalysts to a degradation protocol: 3000 consecutive cycles recorded between 0.6 V and 1.2 V at 100 mV s^{-1} in O_2 saturated 0.1 M HClO_4 . To assess the effects on the Pt particle size, an additional CO_{ad} stripping voltammogram was recorded immediately after the stability tests. The suffix -d identifies the catalysts subjected to the degradation protocol. The CO_{ad} stripping voltammograms are also displayed in Fig. 7 (red lines). The base voltammograms of Pt/CNT10-d and Pt/CNT20-d reveal a severe decrease in the H_{upd} region (only the formation of adsorbed hydrogen is presented) relative to the parent materials, suggesting that the fraction of exposed Pt decreases because the Pt dissolves and/or agglomerates during the degradation test. The shape of the CO_{ad} stripping peak for Pt/CNT10-d reveals two distinct CO_{ad} oxidation peaks with E_{PCO} at 680 and 780 mV. A careful comparison between the CO_{ad} voltammograms of the fresh and degraded Pt/CNT10-t reveals that the lost area accounts for the CO_{ad} oxidation process at lower potentials. Therefore, the Pt particles on Pt/CNT10-d are smaller than before the degradation test, indicating that the Pt particles dissolve to some extent. However, the shape of the CO_{ad} oxidation voltammograms for Pt/CNT20-t and Pt/CNT20-d are identical except that the area of the latter is visible smaller. Therefore, the degradation protocol causes the loss of Pt by dissolution, but the average size of the Pt domains remains nearly identical before and after the degradation test. Finally, the area for the CO_{ad} stripping (and the H_{upd} region) of Pt/CNT60-d is almost identical to the area for the Pt/CNT60 (decreasing only by 8% as shown in Table 2). The shapes of the CO_{ad} peaks recorded before and after the degradation protocol are also very similar; the two peaks shift only 20 mV toward more positive potentials after the degradation test. These results suggest that only a few Pt particles on Pt/CNT-60 dissolved, making it the most stable catalyst in the series.

The stability of the Pt particles subjected to very positive potentials in an O_2 rich atmosphere was determined by their size; larger Pt particles were more stable than the smaller ones [19,44]. However, the stability of the CNT-supported Pt and PtCo particles during thermal treatments in 875°C air increases for the samples prepared on nanotubes containing more surface oxygen species [22,45]. Therefore, the superior stability of the Pt/CNT60-t Pt particles (as demonstrated by lower Pt loss, see Table 2) might be ascribed to both larger Pt particle sizes and amounts of surface oxygen groups in this catalyst.

The size (D) of the Pt particles in both Pt/CNT and Pt/CNT-d catalysts was calculated from the electrochemical surface area (ECSA) values, assuming that the nanoparticles were spherical. The areas

Table 2
Platinum ECSA, % area loss and Pt particle size calculated before and after degradation tests. ORR performance and Pt area-specific activity (i_s) values were obtained at $E=0.90$ V during the negative sweep LSV at 20 mV s^{-1} .

Catalyst	ECSA ($\text{m}^2\text{ g}^{-1}$)	Pt size (nm)	Area loss (%)	ORR Pt area-specific activity (A cm^{-2})
Pt/CNT60-t	19.6	14.3	8.2	0.400
d-Pt/CNT60-t	18.0	15.6		
Pt/CNT20-t	23.2	12.1	21.7	0.286
d-Pt/CNT20-t	18.2	15.4		
Pt/CNT10-t	37.2	7.5	32.2	0.193
d-Pt/CNT10-t	25.2	11.1		

of exposed Pt (ECSA) before and after the degradation tests were calculated by integrating the area of the CO_{ad} stripping peak while assuming that the charge during the electrooxidation of a CO_{ad} monolayer is $420\text{ }\mu\text{C cm}^2$ for Pt [46].

$$D = \frac{6000}{\text{ECSA} \times d} \tag{3}$$

where d is density of Pt (21.45 g cm^{-3}), and ECSA is the electrochemical surface area in $\text{m}^2\text{ g}^{-1}$. The values obtained before and after the stability test are listed in Table 2. Pt/CNT60-t remains the most stable catalyst in the series; its ECSA value remains nearly constant after the degradation tests. However, the ECSA for Pt/CNT10-d and Pt/CNT20-d decreased by ca. 32% and 22%, respectively, after the degradation protocol. Table 2 suggests that the stability of the catalysts was directly related to their particle size in the following order: Pt/CNT60-t > Pt/CNT20-t > Pt/CNT10-t. This result validates the previous observations: the stability of Pt particles increases when deposited on highly functionalized carbon nanotubes, i.e., at the surfaces in which a high amount of oxygen-bearing groups are created [21,22].

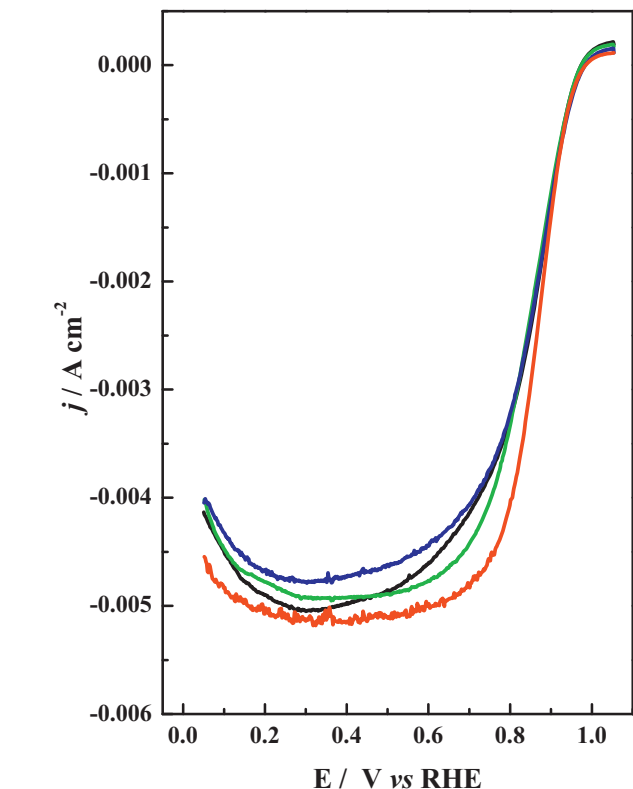


Fig. 8. ORR polarization curves recorded in the positive going scan in O_2 saturated 0.1 M HClO_4 at 20 mV s^{-1} , 1600 rpm for Pt/CNT10-t (black line), Pt/CNT20-t (blue line), Pt/CNT60-t (red line) and 20% Pt/C Commercial Etek (green line). (For interpretation of the references to color in figure legend, the reader is referred to the web version of the article.)

Fig. 8 presents the polarization curves of each Pt/CNT-t recorded at 10 mV s^{-1} in O_2 -saturated 0.1 M HClO_4 .

As expected for carbon-supported Pt nanoparticles [32,47], a kinetic or mixed kinetic diffusion control region was observed between 0.9 V and 0.6 V , in addition to a mass-transfer controlled region at less positive potentials when the limiting current was reached. The onset potential for the ORR was at ca. 980 mV for every catalyst in line with the value expected for Pt-based catalysts. The limiting current values are in line with the theoretical diffusion limiting current indicating a negligible contribution of the O_2 diffusion. The performance of the catalysts is similar although the activity for the ORR seems to increase with the increasing Pt particle size. In order to assess properly the effect of the Pt size for the ORR the data were represented in the Tafel form.

Fig. 9 displays the Tafel slopes for the mass-transport-corrected area-specific current densities for all Pt/CNT-t obtained from the

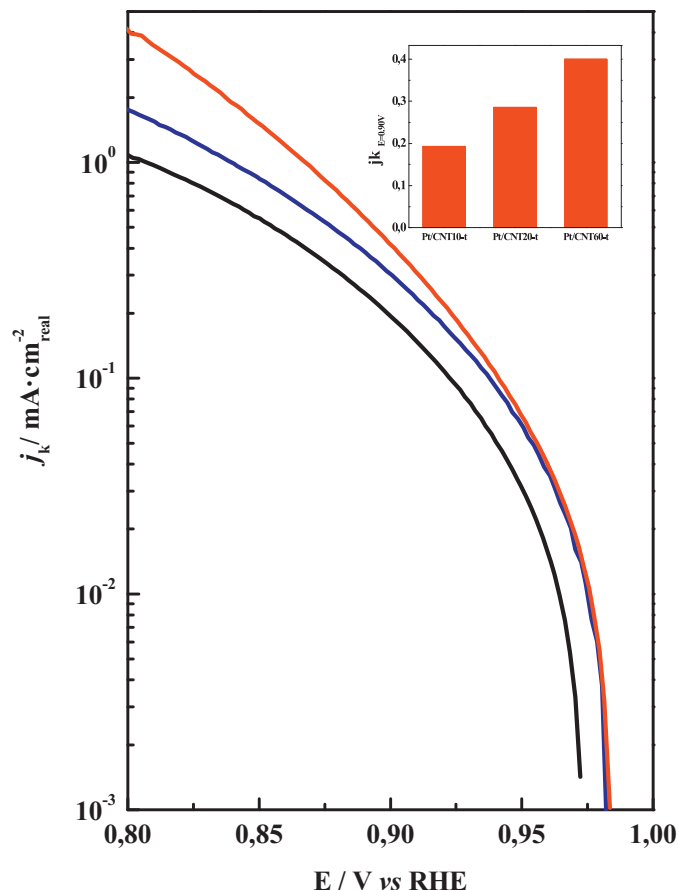


Fig. 9. Tafel plots mass-transport of Pt/CNT10-t (black line), Pt/CNT20-t (blue line), and Pt/CNT60-t (red line) corrected by limiting current and normalized by the Pt area calculated from the CO_{ad} stripping analysis. The inset figure shows the kinetic current density values at 0.9 V . (For interpretation of the references to color in figure legend, the reader is referred to the web version of the article.)

positive sweep at 1600 rpm. The contributions of the pure kinetic currents (j_k) to the total current (j) were deduced using the Koutecky–Levich equation (Eq. (1)), and the current values were normalized to the ECSA values reported in Table 2.

The performance of the catalysts follows a decreasing order throughout the entire polarization range: Pt/CNT60-t > Pt/CNT20-t > Pt/CNT10-t. The current density values at 0.9 V are 0.19, 0.28 and 0.40 mA cm⁻² for Pt/CNT10-t, Pt/CNT20-t and Pt/CNT60-t, respectively (see inset to Fig. 9), agreeing with the reported values for 20 wt.% Pt/carbon Vulcan films [48]. Therefore, the ORR was dominated by Pt particle size effects; larger particles exhibit higher activity during the ORR, validating previous reports [4,42].

4. Conclusions

The results discussed in this paper reveal the strong influence exerted by the diameter of multiwalled carbon nanotubes caused by their specific surface area and the number of anchoring sites, including both C_π and oxygen-bearing groups available after chemical functionalization. The specific surface area increases with the decreasing CNT diameters. However, the number of surface oxygen-bearing groups increases when the nanotubes have increasing diameters. This paper also reveals that the diameter of the CNTs affected the Pt loading and particle size deposited onto treated CNTs. Therefore, both Pt loading and metal dispersion was increased on the nanotubes with smaller diameters, accounting for both the higher specific surface of the nanotubes with the smaller diameters and the increasing number of surface oxygen-containing groups after chemical treatment, particularly the nanotubes with larger diameters. Consequently, the catalytic performances during the ORR and CO_{ad} oxidation were perturbed by the CNT diameter. Moreover, the stability of the Pt particles increased when supported on CNTs with larger diameters (CNT60) because the larger Pt particles and numerous oxygen groups on CNT60-t facilitated stronger interactions between the Pt particles and the support.

Acknowledgements

This project was funded by the Deanship of Scientific Research (DSR), King Abdulaziz University, Jeddah, under grant number (D-006-432). The authors, therefore, acknowledge with thanks DSR technical and financial support. Economic support from projects ENE2010-15381 from the Spanish Ministry of Science and Innovation and Project 201080E116 from the CSIC is also acknowledged.

References

- [1] J.K. Nørskov, J. Rossmeisl, A. Logadottir, L. Lindqvist, J.R. Kitchin, T. Bligaard, H. Jónsson, *J. Phys. Chem. B* 108 (2004) 17886–17892.
- [2] H.A. Gasteiger, S.S. Kocha, B. Sompalli, F.T. Wagner, *Appl. Catal. B: Environ.* 56 (2005) 9–35.
- [3] I.E.L. Stephens, A.S. Bondarenko, U. Grønberg, J. Rossmeisl, I. Chorkendorff, *Energ. Environ. Sci.* 5 (2012) 6744–6762.
- [4] F.J. Perez-Alonso, D.N. McCarthy, A. Nierhoff, P. Hernandez-Fernandez, C. Strebel, I.E.L. Stephens, J.H. Nielsen, I. Chorkendorff, *Angew. Chem. Int. Ed.* 51 (2012) 4641–4643.
- [5] E. Toyoda, R. Jinnouchi, T. Hatanaka, Y. Morimoto, K. Mitsuhashi, A. Visikovskiy, Y. Kido, *J. Phys. Chem. C* 115 (2011) 21236–21240.
- [6] F.T. Wagner, B. Lakshmanan, M.F. Mathias, *J. Phys. Chem. Lett.* 1 (2010) 2204–2219.
- [7] M. Uchida, Y. Aoyama, M. Tanabe, N. Yanagihara, N. Eda, A. Ohta, *J. Electrochem. Soc.* 142 (1995) 2572.
- [8] E. Antolini, *Appl. Catal. B* 88 (2009) 1–24.
- [9] M. Nesselberger, S. Ashton, J.C. Meier, I. Katsounaros, K.J.J. Mayrhofer, M. Arenz, *J. Am. Chem. Soc.* 133 (2011) 17428–17433.
- [10] D. Sebastián, A.G. Ruiz, I. Suelves, R. Moliner, M.J. Lázaro, V. Baglio, A. Stassi, A.S. Aricò, *Appl. Catal. B: Environ.* 115–116 (2012) 269–275.
- [11] N. Job, J. Marie, S. Lambert, S. Berthon-Fabry, P. Achard, *Energ. Convers. Manag.* 49 (2008) 2461–2470.
- [12] V. Selvaraj, M. Alagar, K.S. Kumar, *Appl. Catal. B: Environ.* 75 (2007) 129–138.
- [13] E. Antolini, *Appl. Catal. B: Environ.* 123–124 (2012) 52–68.
- [14] D.R. Kauffman, A. Star, *Analyst* 135 (2010) 2790–2797.
- [15] T. Yoshitake, Y. Shimakawa, S. Kuroshima, H. Kimura, T. Ichihashi, Y. Kubo, D. Kasuya, K. Takahashi, F. Kokai, M. Yudasaka, S. Iijima, *Physica B: Condens. Matter* 323 (2002) 124–126.
- [16] H.-S. Oh, K.H. Lim, B. Roh, I. Hwang, H. Kim, *Electrochim. Acta* 54 (2009) 6515–6521.
- [17] B. Singh, E. Dempsey, *RSC Adv.* 3 (2013) 2279–2287.
- [18] J.C. Meier, I. Katsounaros, C. Galeano, H.J. Bongard, A.A. Topalov, A. Kostka, A. Karschin, F. Schuth, K.J.J. Mayrhofer, *Energ. Environ. Sci.* 5 (2012) 9319–9330.
- [19] F.J. Perez-Alonso, C.F. Elkjær, S.S. Shim, B.L. Abrams, I.E.L. Stephens, I. Chorkendorff, *J. Power Sources* 196 (2011) 6085–6091.
- [20] Y. Shao-Horn, W.C. Sheng, S. Chen, P.J. Ferreira, E.F. Holby, D. Morgan, *Top. Catal.* 46 (2007) 285–305.
- [21] P. Hernández-Fernández, S. Baranton, S. Rojas, P. Ocón, J.-M. Léger, J.L.G. Fierro, *Langmuir* 27 (2011) 9621–9629.
- [22] P. Hernández-Fernández, M. Montiel, P. Ocón, J.L.G. de la Fuente, S. García-Rodríguez, S. Rojas, J.L.G. Fierro, *Appl. Catal. B: Environ.* 99 (2010) 343–352.
- [23] F. Maillard, S. Schreier, M. Hanzlik, E.R. Savinova, S. Weinkauff, U. Stimming, *Phys. Chem. Chem. Phys.* 7 (2005).
- [24] P. Serp, M. Corrias, P. Kalck, *Appl. Catal. A* 253 (2003) 337–358.
- [25] Z.Q. Tian, S.P. Jiang, Y.M. Liang, P.K. Shen, *J. Phys. Chem. B* 110 (2006) 5343–5350.
- [26] J.L. Gómez de la Fuente, S. Rojas, M.V. Martínez-Huerta, P. Terreros, M.A. Peña, J.L.G. Fierro, *Carbon* 44 (2006) 1919–1929.
- [27] J. Ye, J. Liu, Y. Zhou, Z. Zou, J. Gu, T. Yu, *J. Power Sources* 194 (2009) 683–689.
- [28] S. Dong Jin, P. Tae-jin, I. Son-Ki, *Carbon* 31 (1993) 427–435.
- [29] P. Hernández-Fernández, R. Nuño, E. Fatás, J.L.G. Fierro, P. Ocón, *Int. J. Hydrogen Energ.* 36 (2011) 8267–8278.
- [30] J.L.G. de la Fuente, S. Rojas, M.V. Martínez-Huerta, P. Terreros, M.A. Peña, J.L.G. Fierro, *Carbon* 44 (2006) 1919–1929.
- [31] N. Markovic, H. Gasteiger, P.N. Ross, *J. Electrochem. Soc.* 144 (1997) 1591–1597.
- [32] K.J.J. Mayrhofer, D. Strmcnik, B.B. Blizanac, V. Stamenkovic, M. Arenz, N.M. Markovic, *Electrochim. Acta* 53 (2008) 3181–3188.
- [33] J.-P. Tessonier, D. Rosenthal, T.W. Hansen, C. Hess, M.E. Schuster, R. Blume, F. Girgsdies, N. Pfänder, O. Timpe, D.S. Su, R. Schlögl, *Carbon* 47 (2009) 1779–1798.
- [34] A. Peigney, C. Laurent, E. Flahaut, R.R. Bacsa, A. Rousset, *Carbon* 39 (2001) 507–514.
- [35] X. Zhao, W. Li, L. Jiang, W. Zhou, Q. Xin, B. Yi, G. Sun, *Carbon* 42 (2004) 3263–3265.
- [36] J.E. Herrera, D.E. Resasco, *Chem. Phys. Lett.* 376 (2003) 302–309.
- [37] M.A. Pimenta, G. Dresselhaus, M.S. Dresselhaus, L.G. Cancado, A. Jorio, R. Saito, *Phys. Chem. Chem. Phys.* 9 (2007) 1276–1290.
- [38] P. Delhaes, M. Couzi, M. Trinecoste, J. Dentzer, H. Hamidou, C. Vix-Guterl, *Carbon* 44 (2006) 3005–3013.
- [39] P.A. Simonov, V.A. Likhobolov, in: A. Wieckowski, E.R. Savinova, C.G. Vayenas (Eds.), *Catalysis and Electrocatalysis at Nanoparticle Surfaces*, Marcel Dekker, Inc., New York, 2003, pp. 409–454.
- [40] N. Muthuswamy, J.L.G. de la Fuente, P. Ochal, R. Giri, S. Raaen, S. Sundé, M. Ronning, D. Chen, *Phys. Chem. Chem. Phys.* 15 (2013) 3803–3813.
- [41] M. Arenz, K.J.J. Mayrhofer, V.R. Stamenkovic, B.B. Blizanac, T. Tomoyuki, P.N. Ross, N.M. Markovic, *J. Am. Chem. Soc.* 127 (2005) 6819–6829.
- [42] K.J.J. Mayrhofer, B.B. Blizanac, M. Arenz, V.R. Stamenkovic, P.N. Ross, N.M. Markovic, *J. Phys. Chem. B* 109 (2005) 14433–14440.
- [43] F. Maillard, E.R. Savinova, U. Stimming, *J. Electroanal. Chem.* 599 (2007) 221–232.
- [44] K.J.J. Mayrhofer, S.J. Ashton, J.C. Meier, G.K.H. Wiberg, M. Hanzlik, M. Arenz, *J. Power Sources* 185 (2008) 734–739.
- [45] P. Hernández-Fernández, Diseño de electrocatalizadores PtM/C (M = Au, Ru, Co) para la reacción de electroreducción de O₂. Relevancia en pilas de combustible poliméricas alimentadas por hidrógeno o metanol Applied Physical Chemistry (Electrochemistry PhD), Universidad Autónoma de Madrid, 2009.
- [46] P. Stonehart, *J. Appl. Electrochem.* 22 (1992) 995–1001.
- [47] U.A. Paulus, T.J. Schmidt, H.A. Gasteiger, R.J. Behm, *J. Electroanal. Chem.* 495 (2001) 134–145.
- [48] Y. Garsany, O.A. Baturina, K.E. Swider-Lyons, S.S. Kocha, *Anal. Chem.* 82 (2010) 6321–6328.